

A pair of temperate sub-Neptunes transiting the star EPIC 212737443

Mahesh Herath^{1,13*}, Tobias C. Hinse², John H. Livingston³, Jesús Hernández⁴, Daniel F. Evans⁵, Robert Wells⁶, Saraj Gunesechera¹, Jeremy Tregloan-Reed⁷, Markus Rabus^{8,9}, Jesper Skottfelt^{10,12}, Martin Dominik¹¹, Uffe G. Jørgensen¹², Chandana Jayaratne¹³, Cuc T. K. Lý¹⁴

¹ Arthur C. Clarke Institute for Modern Technologies, 0272 Moratuwa, Sri Lanka

² Chungnam National University, Department of Astronomy and Space Science, Daejeon 34134, Republic of Korea (corr. auth.)

³ Department of Astronomy, University of Tokyo, 7-3-1 Hongo, Bunkyo-ku, Tokyo 113-0033, Japan

⁴ Instituto de Astronomía, Universidad Nacional Autónoma de México (UNAM), Ensenada, B.C., Mexico

⁵ Astrophysics Group, Keele University, Staffordshire, ST5 5BG, UK

⁶ Queens University Belfast, University Rd, Belfast BT7 1NN, UK

⁷ Centro de Astronomía (CITEVA), Universidad de Antofagasta, Avenida U. de Antofagasta 02800, Antofagasta, Chile

⁸ Las Cumbres Observatory Global Telescope, 6740 Cortona Dr., Suite 102, Goleta, CA 93111, USA

⁹ Department of Physics, University of California, Santa Barbara, CA 93106-9530, USA

¹⁰ Centre for Electronic Imaging, Department of Physical Sciences, The Open University, Milton Keynes MK7 6AA, UK

¹¹ Centre for Exoplanet Science, SUPA School of Physics & Astronomy, University of St Andrews, North Haugh, St Andrews, KY16 9SS, UK

¹² Niels Bohr Institute & Centre for Star and Planet Formation, University of Copenhagen, Øster Voldgade 5, DK-1350 Copenhagen, Denmark

¹³ Astronomy and space science unit, Department of Physics, University of Colombo 00300, Sri Lanka

¹⁴ Quy Nhon University, Department of Physics, 590-000 Quy Nhon, Socialist Republic of Viet Nam

Accepted XXX. Received YYY; in original form ZZZ

ABSTRACT

We report the validation of a new planetary system around the K3 star EPIC 212737443 using a combination of *K2* photometry, follow-up high resolution imaging and spectroscopy. The system consists of two sub-Neptune sized transiting planets with radii of $2.6R_{\oplus}$ and $2.7R_{\oplus}$, with orbital periods of 13.6 days and 65.5 days, equilibrium temperatures of 536 K and 316 K respectively. In the context of validated *K2* systems, the outer planet has the longest precisely measured orbital period, as well as the lowest equilibrium temperature for a planet orbiting a star of spectral type earlier than M. The two planets in this system have a mutual Hill radius of $\Delta R_H = 36$, larger than most other known transiting multi-planet systems, suggesting the existence of another (possibly non-transiting) planet, or that the system is not maximally packed.

Key words: planets and satellites: detection - techniques: photometric - techniques: spectroscopic - eclipses - individual: EPIC 212737443

1 INTRODUCTION

The *Kepler* mission (Borucki et al. 2010) enabled the discovery of exoplanets at a rate unlike any mission before. The data collected by *Kepler* has uncovered a large variety of planetary systems, with more continuing to be found (e.g. Mayo et al. (2018b)). The *K2* mission utilized the same spacecraft to observe different fields along the ecliptic plane for 80 days each. This time baseline limited the *K2* mission to detecting planets with orbital periods shorter than 45 days on average. Among the small number of confirmed planets with long orbital periods measured by the *K2* mission, the

longest until now was K2-118b (Dressing et al. 2017); this planet has a period of 50.9 days and a size of $2.49R_{\oplus}$. Another long period planet is K2-263b ($2.41R_{\oplus}$) with a 50.8 day orbit (Mortier et al. 2018); K2-263b remains the only planet from the mission with a period greater than 45 days that has a precisely measured mass ($(14.8 \pm 3.1)M_{\oplus}$). The HIP41378 system (Vanderburg et al. 2016b) is thought to contain three planets (planets *d*, *e* and *f*) with likely periods of 156, 131 and 324 days, respectively. Multiple transits were observed for these three planets through *K2* campaigns 5 and 18, though their periods are yet to be precisely determined (Berardo et al. 2018; Becker et al. 2018). The EPIC 248847494 system from *K2* campaign 14 was found to have a single transit event lasting 54 hours, which was revealed to

* E-mail: mherath2@gmail.com

be a possible Jupiter-like planet ($1.11 R_{\text{Jup}}$) through photometric analysis and radial velocity observations (Giles et al. 2018). This object has an estimated orbital period of 3650 days, and is classified as a planet candidate due to having just one observed transit. If confirmed, it would be the longest period transiting exoplanet.

In this work we report the validation of two sub-Neptune sized planets orbiting a K3 type star at a distance of 347 pc. The outer planet of this system has the longest precisely measured orbital period among *K2* planets ($P = 65.5$ days), and this is the only confirmed *K2* multi-planet system with a long period planet showing two or more transits. In section 2, details of the *K2* data reduction and ground-based observations are given. Sections 3.1 and 3.2 outline details of the transit identification and fitting procedure used to characterize each planet candidate. In section 3.3 we review host-star properties as obtained from a previous study. The stellar parameters are derived in sections 3.4 to 3.7. A planet validation analysis by means of a false positive probability is presented in section 4, as well as a dynamical analysis in section 5. The paper is concluded with a discussion of our findings and a summary in sections 6 and 7, respectively.

2 OBSERVATIONS

2.1 *K2* photometry

Due to the failure of two reaction wheels, the *Kepler* spacecraft was re-purposed as the *K2* mission in 2014 (Howell et al. 2014). Recently, in October 2018 the *Kepler* telescope was decommissioned. EPIC 212737443 was observed during *K2* campaign 6 for approximately 80 days between July 13, 2015 and September 30, 2015. Fig. 1 shows a portion of sky centered on the star. The motion of stars over pixels of variable sensitivities caused by the rotation of the spacecraft around its boresight angle can show apparent variations in stellar brightness. A method to remove these systematic variations was devised by (Vanderburg & Johnson 2014), which we will describe in brief. An aperture is placed around the target star, which is defined as either an approximately circular pixel region, or a region of pixels determined by the pixel response function (PRF). The best aperture is found by optimizing the photometric precision of the corrected light curve. The red region in Fig. 2 shows the best aperture chosen in this work and avoids any light contribution from the nearby field star. The flux inside the optimal aperture is decorrelated from position-dependent trends to produce light curves that are available in the Mikulski Archive for Space Telescopes (MAST¹). The target light curve was retrieved from MAST and we removed long-term time dependent trends by fitting and subtracting a cubic spline with knots spaced 0.75 days apart. Fig. 3 shows the raw and detrended *K2* light curve for EPIC 212737443.

2.2 Speckle imaging

Additional data was obtained from the NASA Exoplanet Star and Speckle Imager (NESSI) at the Kitt Peak National

Observatory. We collected data following the procedures described in Howell et al. (2011). Speckle-interferometric observations were conducted simultaneously in the ‘blue’ and ‘red’ bands centred at 562 nm (width = 44 nm) and 832 nm (width = 40 nm) respectively (Scott et al. 2016), at a frame-rate of 25 Hz. After data reduction following Howell et al. (2011), we obtained diffraction limited target images with dimensions of 4.6×4.6 arcseconds (Horch et al. 2009, 2012, 2017). Using concentric annuli centred on the target, we found the background sensitivity limits were estimated as described in Howell et al. (2011). Finally, a contrast curve was produced by fitting a cubic spline to the smoothed 5σ sensitivity limit. The top panel of Fig. 4 shows the contrast curve derived from NESSI observations.

2.3 Lucky imaging

We obtained high-resolution images with a lucky-imaging camera on the night of May 3, 2018 in order to search for nearby stars potentially contributing with contaminating light, as well as detect potential bound companions. The observations were conducted as part of the 2018 MiNDSTEP² campaign using the Two-Colour Instrument (TCI) at the Danish 1.54-m Telescope at ESO/La Silla Observatory. Each TCI consist of a 512×512 pixel Electron Multiplying CCD (EMCCD, Andor, iXon+897) capable of imaging simultaneously in two colours with a field of view (FOV) of about 45×45 arcseconds square. A detailed description of the instrument and lucky imaging reduction pipeline can be found in Skottfelt et al. (2015).

The observations and data reduction were carried out using the method outlined in Evans et al. (2016, 2018), which is briefly described here. The target was observed for 900s at a frame rate of 10 Hz. The raw data were reduced automatically by the instrument pipeline which performs bias and flat frame corrections, removal of cosmic rays, determination of the quality of each frame and frame re-centering with the end product being ten sets of stacked frames ordered by quality. This is then run through a custom star detection algorithm (Evans et al. 2016, 2018) which is designed to detect close companion stars that may not be fully resolved. At this point we would like to stress that due to an observer error the TCI field was centered on the brighter background star EPIC 212737293. This does not however, affect the images. No close companion stars were detected in the lucky imaging data. The only star visible within the TCI FOV is the well-resolved EPIC 212737293 towards the south-east direction at a distance of around 17 arcseconds, and it falls outside the K2SFF pixel aperture. The contrast curve for the LI data can be seen in Figure 4.

2.4 Archival TripleSpec spectroscopy

We used a near-infrared (NIR) spectrum of EPIC 212737443 obtained by Dressing et al. (2017, see their fig. 23) using the TripleSpec instrument (Herter et al. 2008) installed at

¹ <https://archive.stsci.edu/>

² <http://www.mindstep-science.org/>

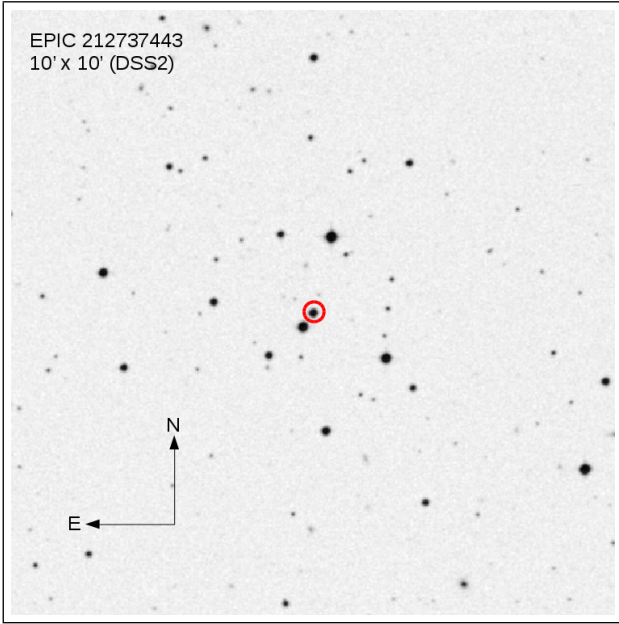


Figure 1. Display of a 10×10 arcmin finder chart of EPIC 212737443 (red circle) obtained from the digital sky survey (DSS2). The star towards south-east is cataloged as EPIC 212737293 and has an angular separation of 17 arcsec. The proper motion of EPIC 212737293 (*Gaia* DR2) is $\mu_\alpha = -2.017 \text{ mas yr}^{-1}$, $\mu_\delta = 0.037 \text{ mas yr}^{-1}$ at a distance of around 2400 pc. Therefore, the two stars are unrelated. See *electronic version for colours*.

the 20-inch Palomar-Hale Telescope. The spectrum was obtained from the ExoFOP-K2³ page for the target star. The spectrograph was operated in the fixed (east-west) 1×30 arcseconds slit-mode yielding a simultaneous coverage of wavelengths between 1.0 and $2.4 \mu\text{m}$ (covering the *YJHK* bands) at a spectral resolution of 2500 to 2700 sampled at 2.7 pixels per resolution element. Core details on the reduction of the spectrum and the corrections that were applied such as the removal of telluric absorption features can be found in Dressing et al. (2017).

2.5 Broad-band archive photometry

We make use of archive photometric archive data spanning the wavelength region from ultra-violet (UV) to infrared (IR). Apparent magnitudes from multi-band photometry are obtained from 2MASS (Skrutskie et al. 2006) [*J, H, K_s*], Pan-STARRS DR1 (Chambers et al. 2016) [*g, r, i, z, y*], Sky-Mapper⁴ (Wolf et al. 2018) [*u, v, g, r, i, z*], ALLWISE (Wright et al. 2010) [*W1, W2, W3, W4*] and *Gaia* DR2 (Gaia Collaboration et al. 2018b) [*G, G_{BP}, G_{RP}*]. All data except for the Sky-Mapper data were retrieved and compiled via the ViZieR service. We note that the AllWISE *W3* and *W4* magnitudes have significantly less photometric precision compared to the other two measurements. In particular the *W4* magnitude is only an upper limit with a signal-to-noise

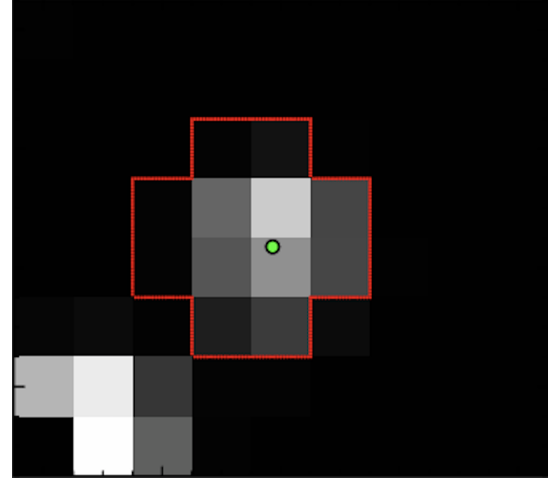


Figure 2. The *K2* image (9×8 pixels) summed from all postage stamp frames of EPIC 212737443 (Vanderburg & Johnson 2014). The image shown is rotated 7.5 degrees east of north (top of the image). Here, the optimal photometric aperture is over-plotted in red around the target, with the green dot indicating the centre of the flux distribution. The nearest field star is located a few *K2* pixels away towards the south-east direction. See *electronic version for colours*.

Table 1. Stellar properties of EPIC 212737443 from the Huber et al. (2017) EPIC stellar classification from *K2* campaigns 1 - 8. Parameter values were obtained from the EPIC catalog retrieved via the VizierR (<http://vizier.u-strasbg.fr/viz-bin/VizieR>) service. We note that the ExoFOP <https://exofop.ipac.caltech.edu/k2> database has incomplete information. The KepFlag=*JHK* indicates the Kepler magnitude K_p was calculated from 2MASS *JHK_s* photometry, which we have repeated in this work in order to derive an uncertainty estimate based on Monte Carlo error propagation.

Parameter	Value	Source
T_{eff} (K)	4542^{+149}_{-298}	Huber et al. (2016)
$\log g$ (cgs)	$4.708^{+0.088}_{-0.040}$	Huber et al. (2016)
radius, R_\star (R_\odot)	$0.57^{+0.040}_{-0.095}$	Huber et al. (2016)
mass, M_\star (M_\odot)	$0.615^{+0.049}_{-0.089}$	Huber et al. (2016)
[Fe/H] (dex)	$-0.473^{+0.300}_{-0.250}$	Huber et al. (2016)
Distance (pc)	$290.8^{+27.3}_{-68.7}$	Huber et al. (2016)
density, ρ_\star (cgs)	$3.22^{+1.49}_{-0.512}$	Huber et al. (2016)
$E(B - V)$ (mag)	$0.037^{+0.035}_{-0.013}$	Huber et al. (2016)
K_p (mag)	14.46 ± 0.13	this work
μ_α (mas/yr)	-54.1 ± 2.5	Huber et al. (2016)
μ_δ (mas/yr)	25.8 ± 3.0	Huber et al. (2016)
catalog s-flag	rpm	Huber et al. (2016)
catalog KepFlag	JHK	Huber et al. (2016)
catalog K-flag	1	Huber et al. (2016)

³ https://exofop.ipac.caltech.edu/k2/edit_target.php?id=212737443

⁴ <http://skymapper.anu.edu.au/>

of less than two. No photometric data from the Sloan Digital Sky Survey (SDSS) exist for EPIC 212737443.

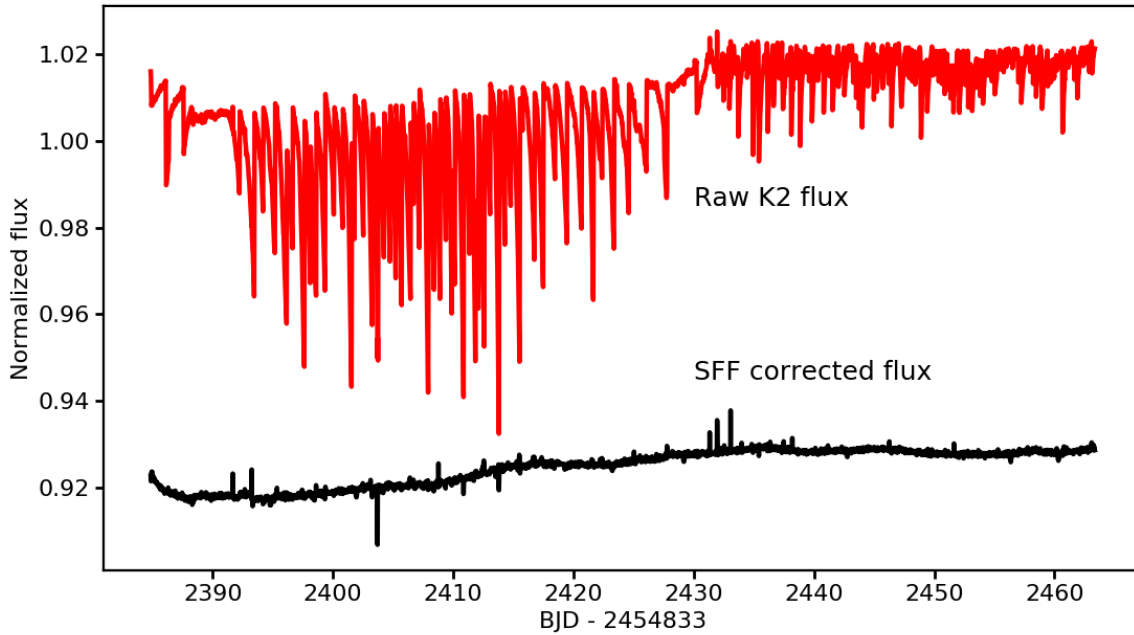


Figure 3. The raw *K2* light curve for EPIC 212737443 (red) with the position dependent trends removed (black) using the methods in Vanderburg & Johnson (2014). See electronic version for colours.

3 DATA ANALYSIS

3.1 Transit detections

A transiting planet candidate with a 13.6 day period was identified in the *K2* light curve by Pope et al. (2016) and again by Barros, Demangeon & Deleuil (2016) for this system. We used the Box Least Square (BLS) algorithm (Kovacs et al. 2002) with a Signal Detection Efficiency (SDE; Ofir (2014)) to confirm the existence of this candidate. The BLS search yielded a 13.6 day signal with a transit depth of 1000 ppm (parts per million) and SDE of 11. We masked the transits identified from the first BLS iteration and ran the BLS algorithm again over the residual data. The second BLS iteration revealed a signal with a period of 65.5 days with $SDE = 7$. Upon visual inspection of the light curve, we identify two transit events at 2394.78 (BJD-2454833) and 2460.44, with each transit having a depth of 1100 ppm.

3.2 Transit modeling

We used the Python package `batman`⁵ (Kreidberg 2015) to model the transits. For computational efficiency, we fitted the models to regions of three transit durations ($3 \times T_{14}$) centred on each transit. The free parameters used to compute the models include; the planet-star radius ratio R_p/R_\star ; the scaled semi-major axis a/R_\star ; the impact parameter $b = a \cos i/R_\star$ where i is the orbital inclination to the line of sight; the epoch of first transit T_0 ; the orbital period P ;

and two limb darkening coefficients (q_1, q_2) from Kipping (2013) assuming a quadratic limb-darkening law. Monte Carlo sampling of the stellar parameters was used to obtain the distributions of the limb darkening coefficients from an interpolated grid based on the tabulated parameters of Claret et al. (2012), which were then used for Gaussian priors on the limb darkening coefficients. The limb darkening coefficients were determined based on stellar atmospheric properties as derived in this work (see section 3.5). Uniform priors were used for all other parameters. In addition we fitted for the logarithm of the Gaussian errors ($\log \sigma$) and a constant out-of-transit baseline offset. For parameter estimation we used an affine-invariant Monte Carlo Markov Chain (MCMC) implemented within the `emcee` Python package (Foreman-Mackey et al. 2013) to sample the posterior distributions of the aforementioned transit model parameters. The MCMC was run for 5000 steps using 100 walkers and a burn-in phase of 2000 steps. We computed the auto-correlation time of each parameter to ensure that we collected at least several thousand effectively independent samples after burn-in. The evolution of the MCMC chain populations were qualitatively monitored by generating trace plots for each parameter. The chains showed convergence after about 600 steps.

The fitted parameters were used to derive the inclination i , and transit duration T_{14} . Initially we did not impose a prior on the stellar density (ρ_\star) and derived its value through the transit fits themselves. The mean stellar densities from the fits for planets b and c were $3.46^{+1.37}_{-2.35}$ and $3.96^{+1.76}_{-2.67}$ g cm^{-3} , respectively. These values are in excellent agreement with each other (0.14σ), and with the independently derived value for mean stellar density of $\rho_\star =$

⁵ <https://www.cfa.harvard.edu/~lkreidberg/batman/>

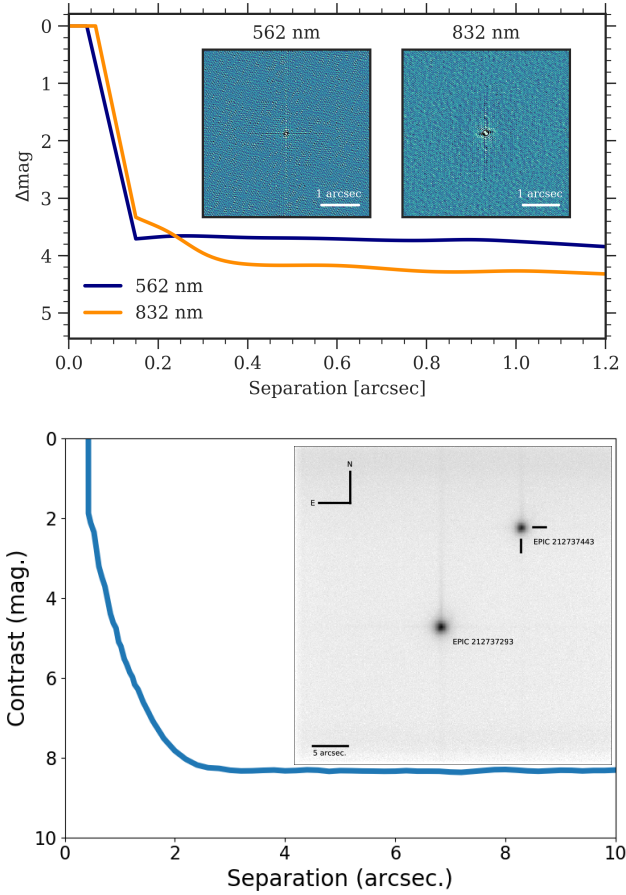


Figure 4. *Top panel:* Contrast sensitivity curve (Δmag) vs separation of EPIC 212737443 from the two reconstructed WIYN/NESSI images (inset). *Bottom panel:* Contrast curve for EPIC 212737443 as obtained from the Danish 1.54-m telescope and spanning a radius of 10 arcseconds from the center (cross-hair). The inset figure (inverse logarithmic scale) shows the 45×45 arcseconds TCI field of view (red camera) including the nearest star EPIC 212737293 located at a distance of about 17 arcseconds. See *electronic version for colours*.

$3.190^{+0.256}_{-0.250} \text{ g cm}^{-3}$. We repeated our parameter estimation calculations with a Gaussian prior based on the stellar density derived in section 3.8. In addition, we did not detect any Transit Timing Variations (TTVs) in this system. Figure 5 gives the folded light curves with their respective best fit models for planets *b* and *c*. We report the median and 68% credible interval of the resulting posteriors.

For planet *c*, we fitted each transit separately, using a uniform prior for the orbital period and assuming both circular and eccentric orbits. We then compared the resulting posteriors from each fit. The duration and depth agreed to within 0.06σ and 0.27σ for all posteriors (both eccentric and circular orbits). When we then repeated the experiment using a Gaussian prior on the mean stellar density, based on our result in Table 3. In this case, the posterior distribution of the orbital period peaked near 65 days. Under the assumption that the transits are from two different objects, we then computed the minimum orbital periods necessary

to replicate the observations in our data. Using the mid-transit time of each eclipse with the start and end points of the photometry, we determined that the shortest period which would show a single transit is 68.6 days. We then used the radius derived for each transit to estimate planet masses via the empirical mass-radius relationship of Weiss & Marcy (2014). Following Weiss et al. (2018) we found the ratio of periods (P_2/P_1) corresponding to a Mutual Hill radius of 3.5, which is the theoretically determined stability criterion for the minimum space between two planets (Wisdom 1980). This presented a scenario in which two equally-sized planets with periods of 68.6 and 80.2 days can recreate the two transits seen in our data-set. Assuming that these orbits are circular ($e = 0$) with equatorial transits ($b = 0$), we computed the transit durations using the periods and their semi-major axes. The durations were larger (0.2320 ± 0.06 and 0.2450 ± 0.07 days) by a factor of 0.68σ and 0.72σ than the durations of the observed transits (0.190 ± 0.016 and 0.192 ± 0.022 days). The durations differ by a factor of 0.15σ between transits as opposed to the 0.06σ difference in our observed transits. However the durations become indistinguishable between orbits for values of $e > 0$ and $b > 0$.

3.3 Preliminary stellar classification

An initial characterization of EPIC 212737443 was presented by Huber et al. (2017) based on the classification of 138,600 stars in *K2* campaigns 1 - 8. The result constitutes the Ecliptic Plane Input Catalog (EPIC⁶). The single-star characterization is based on a simulated synthetic stellar population obtained from the *Galaxia* model (Sharma et al. 2011). The model is obtained by means of calibration of the observed *J*-band distribution of a sample of targets in the *Kepler* field with well-determined stellar properties obtained from asteroseismology and spectroscopy Huber et al. (2014). Stellar properties are then inferred from posterior probabilities using the synthetic stellar population as a prior in conjunction with archive broad-band photometry and kinematics for each catalog star. Stellar masses are predicted from interpolation of tabulated isochrones obtained from the *Padova* stellar evolution database. Stellar properties of EPIC 212737443 as obtained by Huber et al. (2017) are listed in Table 1. The characterization of EPIC 212737443 makes use of the reduced proper motion Gould & Morgan (2003) and 2MASS *JHK_s* photometry (Skrutskie et al. 2006). We find the *J*–*K_s* color to be 0.664 ± 0.035 . The *J*-band reduced proper motion (RPM_J) is calculated to be 6.373 ± 0.026 mag using recent *Gaia* DR2 astrometry data (Section 3.4). Qualitatively, the (*J* – *K_s*, RPM_J) measurements classifies EPIC 212737443 as a dwarf-star (Huber et al. 2017, see their fig. 6). For this particular population, $\log g$ seems to be well constrained to within a relatively narrow interval of $\log g \in [3.5, 5]$ with T_{eff} spanning from 3500 to 8000 K. These parameter ranges are consistent with what is expected for dwarf stars from theoretical considerations.

We note that Huber et al. (2017) discussed several short-comings in their method. The source of largest bias

⁶ <http://vizier.u-strasbg.fr/viz-bin/VizieR?-source=J/ApJS/224/2>

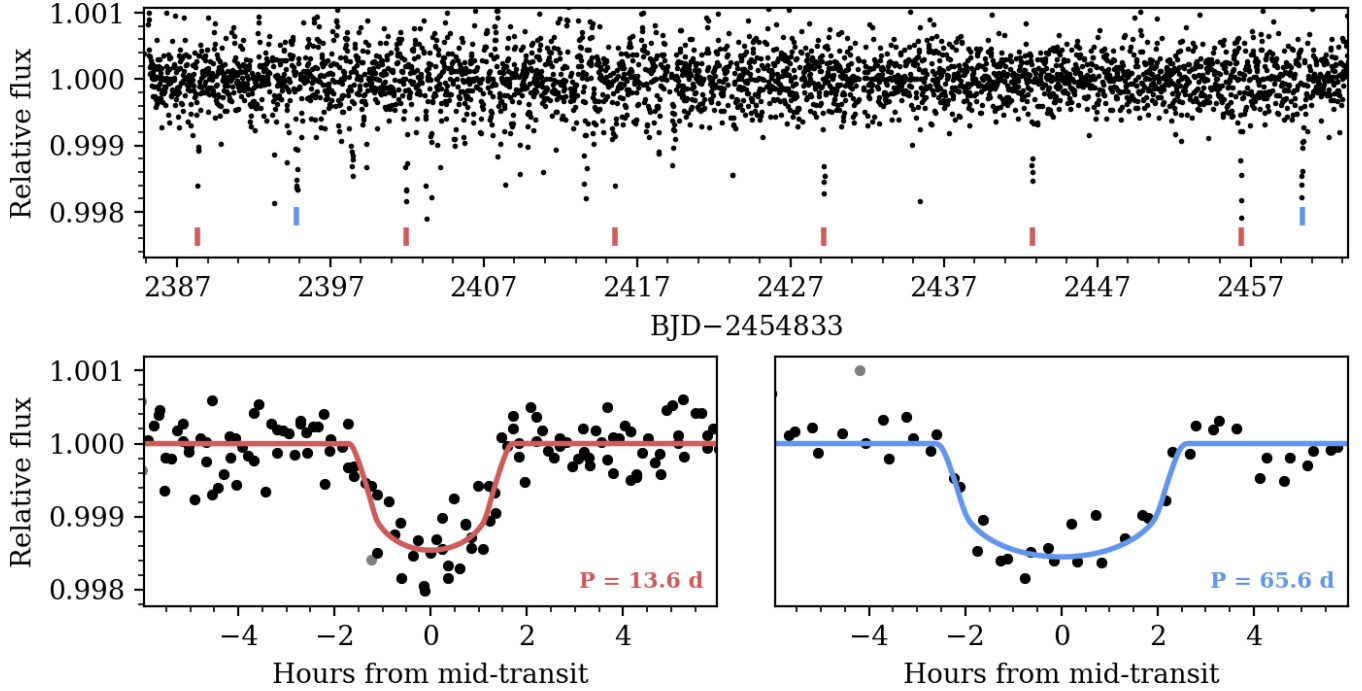


Figure 5. *Top panel:* The reduced light curve for EPIC 212737443 with the transits marked using red and blue ticks. *Bottom panels:* The phase-folded transit for each planet overlaid with the best-fitting transit model in red and blue for planets b and c respectively. See *electronic version for colours*.

in stellar mass and radius is the use of slightly outdated isochrones that were adopted in the *Galaxia* model. Huber et al. (2017) reports that inferred stellar radii of K- to M-type dwarf stars can be underestimated by up to 20%. Dressing et al. (2017) presents near-infrared spectroscopic follow-up observations of 144 candidate planetary systems from *K2* campaigns 1 - 7, including 72 near-infrared spectra of cool dwarfs ($T_{\text{eff}} < 4800 \text{ K}$ and $R_{\star} < 0.8 R_{\odot}$). While their revised effective temperatures are generally consistent with the statistically inferred temperatures from Huber et al. (2017) the authors find that stellar radii are typically $0.13 R_{\odot}$ larger. Hence the Huber et al. (2017) EPIC catalog is only a preliminary resource for estimation of stellar properties. From sections 3.4 to 3.8 we attempt to derive stellar properties from archive photometry and a single near-infrared spectrum.

3.4 Astrometry and stellar kinematics

From *Gaia* DR2 (Gaia Collaboration et al. 2018b) the parallax of EPIC 212737443 was measured to be $\pi = 2.95 \pm 0.04 \text{ mas}$ (relative error of $\sigma_{\pi}/\pi \approx 1.4$ percent). From $d = 1/\pi$ along with a Monte Carlo based error propagation we find that $d = 339.5 \pm 4.8 \text{ pc}$. Using Luri et al. (2018) and the Bayesian-based method for distance estimation outlined in Kupfer et al. (2018), we found that $d = (338.0 \pm 4.9) \text{ pc}$, which is in good agreement (0.22σ) within of our distance estimate. In general, for measurements with a relative parallax error of < 10 percent the distance estimate from a Bayesian inference is nearly identical to a $1/\pi$ distance estimate and mainly independent of the choice of prior (Bailer-Jones et al. 2015). EPIC 212737443 has *Gaia* DR2 proper motions in RA and Dec of -46.2 and 22.2 mas yr^{-1} , respectively. The total

proper motion is 51.3 mas yr^{-1} . Combining the proper motion and *Gaia* distance results in a tangential velocity of approximately 82 km s^{-1} . From our TripleSpec spectrum, we measured the radial velocity of the star to be $(-16 \pm 5) \text{ km s}^{-1}$. By combining the total proper motion, distance and radial velocity, we found a 3-D space velocity of $(U, V, W) = (89.6, -8.7, 27.1) \text{ km s}^{-1}$ relative to the local standard of rest (LSR), assuming a Solar motion of $(10.0, 5.3, 7.2) \text{ km s}^{-1}$ from Dehnan & James. (1998).

It is possible to infer the Galactic population of a star from the 3-D kinematics (see Soubiran et al. (2003) and Bensby, Feltzing & Lundström (2003)). Following the method of Reddy, Lambert & Allende Prieto (2006), we obtain population probabilities of 92, 8 and $< 0.1\%$ for the thin disk, thick disk and halo populations, respectively. We note that there are uncertainties in the derived velocities and Solar motion, however these only affect the probabilities by a few percent. We therefore suggest EPIC 212737443 is a member of the Galactic thin disk.

3.5 Stellar temperature and surface gravity

We derived stellar atmospheric properties by comparing the reduced TripleSpec spectrum to synthetic spectra from the Phoenix (Husser et al. 2013) library of high resolution spectra. All library spectra were downgraded by convolution to match the spectral resolution of the TripleSpec spectrum. The library considers stars with $2300 < T_{\text{eff}} < 15000 \text{ K}$ and $0 < \log g < 6$ (cgs). The TripleSpec spectrum was normalized with a second order polynomial function. We implemented an IDL routine which randomly selects 25 points for each band from the continuum level (within 2% of the continuum) and then tested against library spectra which

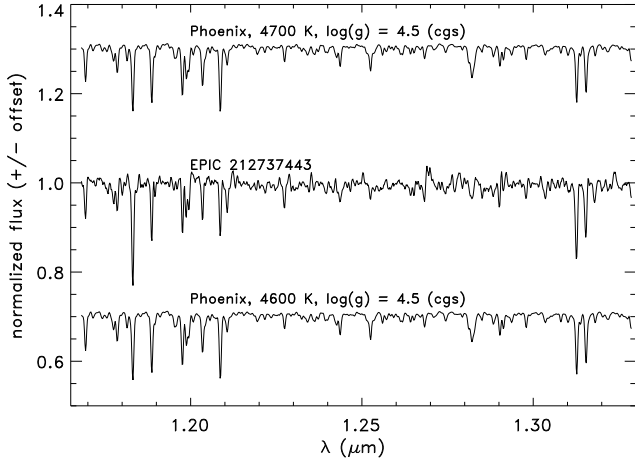


Figure 6. Observed and normalized J -band TripleSpec spectrum of EPIC 212737443 (middle) compared to Phoenix synthetic spectra fixed at $\log g = 4.5$ (cgs).

were normalized with a polynomial using the random points found for the target spectrum. We systematically probed $2300 < T_{\text{eff}} < 15000$ K with *i*) $\log g$ freely varying and *ii*) $\log g = 4.5$ (cgs) and *iii*) $\log g = 5.0$ (cgs), and we evaluated the χ^2 statistic to quantify each match. A best-fit Gaussian function was fitted to the resulting distribution providing a mean and uncertainty. As a test of our method, we downloaded the reduced TripleSpec spectrum for the star EPIC 211770795 (Dressing et al. 2017) and compared the Dressing-derived temperature ($T_{\text{eff}} = (4753^{+129}_{-155})$ K) to the value obtained through our method ($T_{\text{eff}} = (4589 \pm 189)$ K). The values were in good agreement (0.67σ), and was based on fixing $\log g = 4.5$ (cgs). No significant variation was seen when varying $\log g$ by ± 0.5 . We therefore base our results on the Phoenix library with $\log g = 4.5$ (cgs), and for EPIC 212737443 we found $T_{\text{eff}} = (4635 \pm 110)$ K. This estimate agrees well with the EPIC catalog at a 0.29σ level. A surface gravity of $\log g = 4.5$ (cgs) is consistent with the results from the EPIC catalog (see section 3.3).

3.6 SED modeling

To get a second independent set of values for T_{eff} and $\log g$, we compiled all available observed archive (reddened) broadband photometric measurements (see Table 2) for our target and carried out a spectral energy distribution (SED) analysis. We used the Virtual Observatory SED Analysis (VOSA⁷ v5.1) tool (Bayo et al. 2008) for this purpose. VOSA derives stellar properties by using theoretical atmosphere models from which synthetic photometry is calculated to fit the observed stellar magnitudes in various pass-bands. We considered the BT-Settl atmosphere model (Allard et al. 2012) for which grid models exist for a large range in the three main atmospheric parameters.

The effect of interstellar extinction was accounted for in the SED modeling by adopting the mean extinction law for interstellar dust $R_V = 3.1 \pm 0.1$ as described by Fitzpatrick (1999). The colour excess $E(B - V)$ was obtained from the

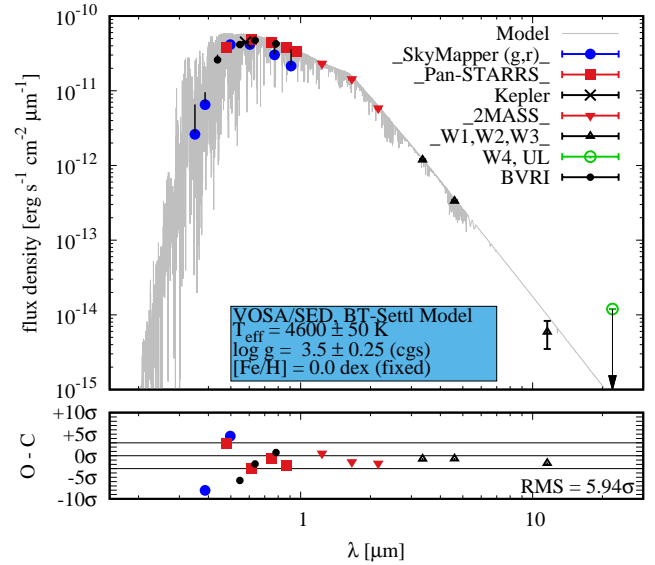


Figure 7. Spectral energy distribution ($\log(F_\lambda)$) as obtained from VOSA. The SED is obtained from the BT-Settl atmosphere model. Filter characteristics were taken from the SVO (Spanish Virtual Observatory) filter profile service: <http://ivoa.net/documents/Notes/SVOFPS/index.html>. The reduced χ^2_ν was found to be 50.93. Data points are de-reddened. For some data points the error-bar is smaller than the symbol size. Horizontal lines in the residual plot indicate $\pm 3\sigma$ levels

. See electronic version for colours.

Bayestar15⁸ sight-line 3D dust map provided by Green et al. (2015) using the distance inferred from *Gaia* DR2. We determined $E(B - V) = 0.01^{+0.02}_{-0.01}$. The resulting extinction was found to be in the range $A_V \in [0, 0.083]$. This reddening is somewhat consistent with the value (0.04) found by Huber et al. (2017) and is concordant with the *K2* Campaign 6 field of view being outside the galactic plane, where reddening in general is expected to be small. The five model parameters were T_{eff} , $\log g$, $[\text{Fe}/\text{H}]$, A_V and M_d , where the latter parameter is a flux density proportionality factor. The *Gaia* parallax distance to EPIC 212737443 was included in the SED analysis to obtain an estimate of the stellar radius from the derived total flux estimate. For EPIC 212737443 the 2MASS JHK_s photometry in particular is of great value to constrain T_{eff} due to probing different slopes on the SED. We chose to discard the u, v, i, z SkyMapper measurements since they consistently underestimate the theoretical flux densities. They are discrepant at a $> 10\sigma$ level. Including SkyMapper (u, v, i, z) data produced fits with χ^2_ν typically larger than 200. Also the *Gaia* measurements were not included as the three spectral windows are too broad. Derived photometric pass-bands including the *Kepler* and the AllWISE W4 (upper limit magnitude only) magnitudes were also not included in the final SED analysis. Table 2 indicate which data were used in the SED analysis.

Initially we let all model parameters float freely. Based on the BT-Settl model we found values of $T_{\text{eff}} = (4600 \pm 50)$ K, $\log g = (4.5 \pm 0.35)$ cgs and $[\text{Fe}/\text{H}] = (-1.0 \pm 0.25)$ dex. The reduced chi-squared χ^2_ν was found to be 34.3 for (13 - 5) degrees of freedom. As a rule of thumb (C. Rodrigues, priv.

⁷ <http://svo2.cab.inta-csic.es/theory/vosa>

⁸ <http://argonaut.skymaps.info/>

Table 2. Stellar parameters of EPIC 212737443. We derived the Johnson-Cousins (B_J, V_J) and Kron-Cousins (R_C, I_C) magnitudes from the precise Pan-STARRS1 g_{P1}, r_{P1}, i_{P1} magnitudes as a weighted mean using the linear transformation equations from [Tonry et al. \(2012\)](#) and [Kostov & Bonev \(2018\)](#). The derived magnitudes however were not included in the SED modeling. For all considered models we find that the SkyMapper u, v and i, z flux densities are systematically underestimated when compared to the model-based flux densities. We indicate those points with vertical lines in Fig. 7. The acclaimed precision in those pass-bands seems too high and the associated errors are likely much larger in reality. We have therefore excluded the SkyMapper u, v, i, z data and found models with a significantly smaller χ^2_ν on the order of $\chi^2_\nu \approx 30$. We **highlight** data that were included in the SED modeling.

Parameter	Value	Source
Astrometry		
α_{J2000} R.A. (hh:mm:ss)	13:36:53.21	<i>Gaia</i> DR2
δ_{J2000} Dec. (dd:mm:ss)	-07:19:05.32	<i>Gaia</i> DR2
π (mas)	2.95 ± 0.04	<i>Gaia</i> DR2
Photometry		
u (mag, 3490 Å)	17.731 ± 0.029	SkyMapper
v (mag, 3840 Å)	17.324 ± 0.055	SkyMapper
g (mag, 5100 Å)	15.113 ± 0.005	SkyMapper
r (mag, 6170 Å)	14.494 ± 0.010	SkyMapper
i (mag, 7790 Å)	14.084 ± 0.003	SkyMapper
z (mag, 9160 Å)	13.940 ± 0.016	SkyMapper
g_{P1} (mag, 4866 Å)	15.2645 ± 0.0025	Pan-STARRS1
r_{P1} (mag, 6215 Å)	14.4375 ± 0.0039	Pan-STARRS1
i_{P1} (mag, 7545 Å)	14.1158 ± 0.0040	Pan-STARRS1
z_{P1} (mag, 8679 Å)	13.9720 ± 0.0009	Pan-STARRS1
y_{P1} (mag, 9633 Å)	13.8671 ± 0.0027	Pan-STARRS1
G (mag)	14.481 ± 0.001	<i>Gaia</i> DR2
G_{BP} (mag)	15.087 ± 0.003	<i>Gaia</i> DR2
G_{RP} (mag)	13.743 ± 0.004	<i>Gaia</i> DR2
J (mag, 1.26 μm)	12.824 ± 0.026	2MASS
H (mag, 1.60 μm)	12.239 ± 0.026	2MASS
K_s (mag, 2.22 μm)	12.160 ± 0.024	2MASS
$W1$ (mag, 3.4 μm)	12.093 ± 0.023	AllWISE
$W2$ (mag, 4.6 μm)	12.149 ± 0.023	AllWISE
$W3$ (mag, 12.0 μm)	12.609 ± 0.442	AllWISE
$W4$ (mag, 22.0 μm)	9.074 (see text)	AllWISE
Derived photometry		
B_J (mag)	15.963 ± 0.0034	this work
V_J (mag)	14.836 ± 0.013	this work
R_C (mag)	14.191 ± 0.016	this work
I_C (mag)	13.626 ± 0.017	this work
K_P (mag)	14.46 ± 0.13	this work

comm.) good SED models have $10 < \chi^2_\nu < 50$. Errors were found from a Monte Carlo bootstrapping method and are mainly limited by the grid mesh for a given parameter. The surface gravity is consistent with the ($J - K_s, \text{RPM}_J$) measurement for our star (see section earlier). The most accurate parameter from a SED model is the T_{eff} . However, in our case an uncertainty of 50 K is judged to be too optimistic. The surface gravity and metallicity are in general poorly con-

strained from broad-band photometry and are therefore the least accurate quantities. In our second experiment, we fixed the metallicity to $[\text{Fe}/\text{H}] = 0.0$ dex, since a $[\text{Fe}/\text{H}] = -1.0$ dex is rarely found for stars in the solar neighborhood. Fixing the metallicity to a solar value is empirically justified following the work by [Guo et al. \(2017\)](#). The authors found a mean metallicity of $[\text{M}/\text{H}]_{\text{mean}} = (-0.045 \pm 0.009)$ dex from a sample of ≈ 800 Kepler target stars. This value is significantly (3.8σ) larger than the metallicity estimate from the first SED experiment for a freely floating metallicity. Based on the BT-Settl model we found values of $T_{\text{eff}} = (4600 \pm 50)$ K, $\log g = (3.5 \pm 0.25)$ cgs for a fixed $[\text{Fe}/\text{H}] = 0.0$ dex. The reduced chi-squared χ^2_ν was found to be 50.9 for (13 - 4) degrees of freedom. While the effective temperature has not changed (with a possibly too optimistic uncertainty); the surface gravity changed by 2.3σ between the two runs.

From the distance, total flux and effective temperature, as obtained from the second experiment, the stellar radius is found to be $R_\star = (0.660 \pm 0.019) R_\odot$. From the surface gravity and the radius estimate, we find an *unreliable* stellar mass of $M_\star = (0.050 \pm 0.029) M_\odot$ and should be ignored. The SED produced from VOSA is shown in Fig 7. In a final attempt we tried to estimate the stellar metallicity from considering various evolutionary tracks ([Siess et al. 2000](#)) in a colour-absolute-magnitude diagram. We found the uncertainties in the absolute magnitude to be too high in order to constrain the metallicity for this star. For the remainder of this work we therefore adopt a metallicity estimate of $[\text{Fe}/\text{H}] = 0.0$ dex as suggested empirically by [Guo et al. \(2017\)](#).

3.7 Stellar mass and radius - I

To obtain estimates for the stellar mass and radius, we used the method outlined in ([Da Silva et al. 2006](#)) made available via the PARAM⁹ (v 1.3) web interface service. Stellar parameters are interpolated from stellar isochrones constrained by the bolometric luminosity and effective temperature. The luminosity is determined from *Gaia* DR2 parallax and the extinction corrected V band magnitude which we calculated from JHK_s photometry using the method in [Huang & Hartman et al. \(2015\)](#). We used the previously (second SED experiment) determined values of $T_{\text{eff}}, [\text{Fe}/\text{H}] = 0.0$ and $m_V = (14.836 \pm 0.013)$ along with $\pi = (2.95 \pm 0.04)$ mas as input values, and found $M_\star = (0.713 \pm 0.012) M_\odot$, $R_\star = (0.658 \pm 0.008) R_\odot$, $\log g = (4.633 \pm 0.015)$ cgs. The radius estimate is in excellent agreement (0.1σ level) with the radius estimate obtained from the second SED run.

3.8 Stellar mass and radius - II

To produce a final set of parameters, we used the **isochrones** ([Morton 2015a](#)) Python interface to the MIST stellar evolution models ([Dotter 2016](#)). The parameters are calculated with the 2MASS JHK_s band photometry and *Gaia* DR2 parallax measurements. Initially we used Gaussian priors on T_{eff} and $\log g$ based on our results from section 3.5, and posterior samples via the MULTINEST algorithm ([Feroz et al. 2013](#)). We found that $T_{\text{eff}} = (4684 \pm 79)$ K, $\log g = (4.622 \pm 0.024)$ cgs, $[\text{Fe}/\text{H}] = -(0.137 \pm 0.127)$ dex, $M_\star = (0.690 \pm 0.038) M_\odot$,

⁹ http://stev.oapd.inaf.it/cgi-bin/param_1.3

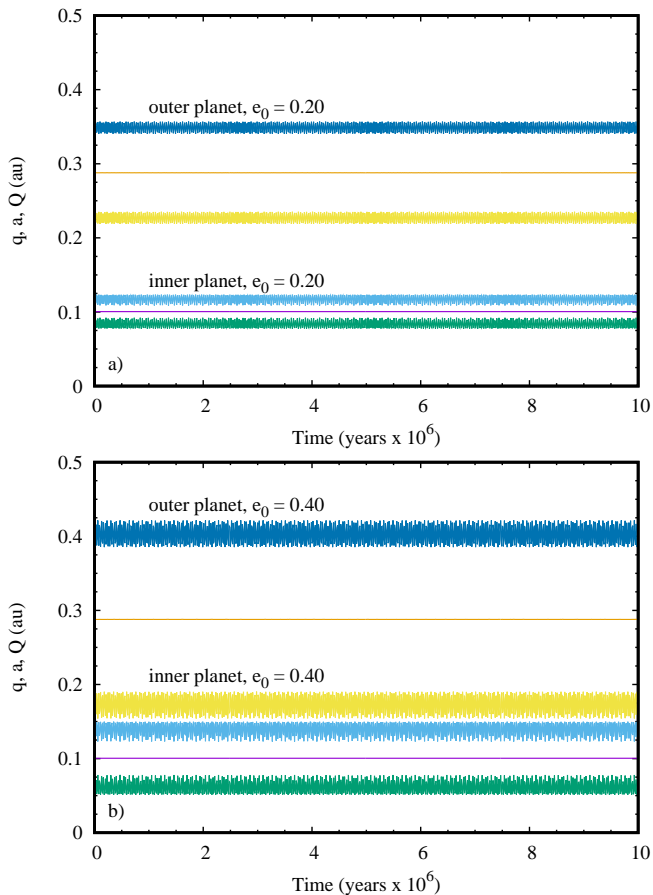


Figure 8. Time evolution of pericentre distance (q), semi-major axis (a) and apocentre distance (Q) for the two transiting planets considering a 10^7 year integration. Results for two initial eccentricities are shown. See *electronic version for colours*.

$R_{\star} = (0.673 \pm 0.024) R_{\odot}$, and $A_V = 0.150^{+0.186}_{-0.108}$ magnitudes. We then removed the priors on T_{eff} and $\log g$ to get another set of values using only the broadband photometry and *Gaia* DR2 parallax. No change was seen between the outputs, except the metallicity which had a value of $[Fe/H] = -(0.180 \pm 0.124)$ dex in the second run. We also found that the mean stellar density $\rho_{\star} = 3.190^{+0.256}_{-0.250}$ which is in good agreement with the values derived in Section 3.2. We used this value of the mean density as a prior in the transit analysis (see section 3.2). The final parameters are given in Table 3.

4 STATISTICAL VALIDATION

An assessment of the probability that the transits are astrophysical false positives was conducted using the VESPA software package (Morton 2015b). VESPA utilizes the Trilegal galaxy model (Girardi et al. 2005) to determine the posterior probabilities for planetary scenarios and a set of false positive scenarios. The false positive scenarios taken into account include; a blended background eclipsing binary; a hierarchical triple system; the star is an eclipsing binary. All these scenarios are simulated by modeling the host star and its background, which are then compared to

Table 3. Adopted physical and atmospheric parameters for EPIC 212737443 using isochrones (Morton 2015a).

Parameter	Value	Source
T_{eff} (K)	4684 ± 79	this work
$\log g$ (cgs)	4.622 ± 0.024	this work
$[Fe/H]$ (dex)	-0.137 ± 0.127	this work
R_{\star} (R_{\odot})	0.673 ± 0.024	this work
M_{\star} (M_{\odot})	0.690 ± 0.038	this work
Distance (pc)	347.449 ± 12.014	this work
A_V (mag)	$0.150^{+0.186}_{-0.108}$	this work
ρ_{\star} (g/cm^3)	$3.190^{+0.256}_{-0.250}$	this work

the observed phase-folded light curve. VESPA uses the broadband photometric data, spectroscopic priors and the contrast curves described in Section 2 as input. Additionally we use the physical parameters of the planets and host star as calculated in Section 3, and constraints on the secondary eclipse depth and maximum exclusion radii. We use the criterion that if the false positive probability (FPP) is $< 1\%$ then the planet is considered validated (Montet et al. (2015); Crossfield et al. (2016)). For this system, VESPA returned FPP values of 4.79×10^{-5} and 1.15×10^{-8} for planets b and c , respectively. Candidates in multi-transiting systems are much more likely to be planets than those in single transit systems (Lissauer et al. 2012), which VESPA does not take into account. It was estimated that candidates in systems with two transits are 25 times more likely to be planets, thus the true FPPs are likely even lower than the above estimates from VESPA. We therefore consider this to be a validated system of two planets.

5 DYNAMICAL STABILITY

We carried out a dynamical stability analysis based on the probabilistic mass-radius relation of Wolfgang et al. (2016). Using the mass-radius relation, the planet masses were found to be $(9.24 \pm 2.64) M_{\oplus}$ and $(9.63 \pm 2.58) M_{\oplus}$, for b and c respectively. We employed the MERCURY6 orbit integration package (Chambers 1999) and utilized the mixed-variable symplectic (MVS) algorithm with a constant time stepping of 1/10 days. We integrated several initial orbital configurations aiming at investigating the orbital stability as function of the initial phase and eccentricity. Co-planar orbits were considered. The initial semi-major axis values were set to the derived values obtained from the best-fit model. Several orbital configurations were integrated for 10^5 years. Long-term integration spanned a time period of 10^7 years. After integration, the relative energy change was at the order of a few part in 10^9 . The results are shown in Fig. 8a to Fig. 8c. We chose to display the time evolution of the pericentre distance ($q = a(1 - e)$), semi-major axis (a) and apocentre distance ($Q = a(1 + e)$) for various eccentricities of the two planets providing information on the eccentricity variation. System stability for the two-planet system is demonstrated for low to moderate initial eccentricities from 0.0 up to 0.40 for both planets. The system became unstable at eccentricities over 0.40, implying the onset of orbit crossing between the two planets, thus imposing a constraint on the eccentricities that are possible for each planet. For initial circular

Table 4. Final best-fit and derived parameters for the two planets in the EPIC 212737443 system.

Parameter (units)	212737443 <i>b</i>	212737443 <i>c</i>
Model parameters		
$T_0 - 2457000.0$ (BJD)	234.970 ± 0.004	227.790 ± 0.005
P (days)	13.6030 ± 0.0013	65.5500 ± 0.0089
R_p/R_\star	0.0352 ± 0.0012	0.0366 ± 0.0016
b	0.479 ± 0.101	0.567 ± 0.082
a/R_\star	31.994 ± 0.646	91.172 ± 1.820
q_1	0.626 ± 0.025	0.626 ± 0.025
q_2	0.105 ± 0.019	0.105 ± 0.019
Derived parameters		
a (au)	0.098 ± 0.004	0.280 ± 0.006
R_p (R_\oplus)	2.586 ± 0.126	2.690 ± 0.146
M_p (M_\oplus)	9.24 ± 2.64	9.63 ± 2.58
T_{14} (days)	0.124 ± 0.005	0.192 ± 0.010
i ($^\circ$)	89.071 ± 0.161	89.630 ± 0.044
T_{eq} (K)	536 ± 18	316 ± 10

and near-circular orbits the mutual perturbations are small for the considered masses and the system stability is qualitatively guaranteed over the 10^7 years. Mutual gravitational perturbations seem small for the considered masses.

6 DISCUSSION

In the context of *K2* exoplanets, planet *c* has the longest confirmed orbital period with two or more observed transits¹⁰. The HIP41378 system is thought to contain three planets with orbital periods above 100 days (Vanderburg et al. 2016b), but are yet to be precisely measured (Berardo et al. 2018); Becker et al. (2018)).

Using the equation $T_{\text{eq}} = T_*(R_*/2a)^{1/2}[f(1 - A_B)^{1/4}]$, and applying $f = 1$ (Koch et al. 2010) with a bond albedo of $A_B = 0.3$, we find the equilibrium temperatures of planets *b* and *c* to be 536 ± 18 K and 316 ± 9 K respectively, making them both temperate planets. Again, planet *c* stands out as the coolest planet found around a star earlier than an M-type star within the *K2* mission¹¹.

Since planet *c* only exhibits two transits, there is a non-zero probability that the transits are from two distant planets as opposed to being from a single body (Benneke et al. 2017). In Section 3.2 we showed that when the two transits are taken individually, they have near-identical transit depths and transit durations. In addition we demonstrated that if the transits are from two separate objects with circular, equatorial orbits, they would have minimum periods of 68.6 and 80.2 days with transit durations longer than what was observed. We carried out an additional investigation to determine the transit durations if these orbits are eccentric with non-zero impact parameters. We found that the theoretical durations become more consistent with the observed durations for values of b between 0.45 and 0.6,

eccentricities between $e = 0.25$ and $e = 0.4$. If the orbits are moved further away from each other, stable orbits with a high eccentricity that could replicate the observed data become more likely. Therefore we acknowledge the possibility that the two transits spaced 65 days apart could be from two different bodies. But based on our analysis, a two planet system with planet *c* having a period of 65 days seem the simpler explanation for the observations. The current ephemeris of planet *c* could be used to predict when future transits would happen, and targeted observations could be carried out at a specific time with a telescope such as the *Spitzer Space Telescope* or CHEOPS. The observation of a third transit at a predicted time would confirm if the two transits seen in our data belong to the same object.

We computed the mutual Hill radius (ΔR_H) between the two planets using the methods in Weiss et al. (2018). As the mutual Hill radius is dependent on the planet masses, we used both the empirical relationship in Weiss & Marcy (2014) as well as the relationship in Wolfgang et al. (2016), and found $\Delta R_H = 33.1$ and 36.2 respectively. Similarly, we found the values of ΔR_H for all adjacent pairs of planets validated throughout the *K2* campaign. The distribution of ΔR_H was consistent between the values of 10 and 30 (with the Weiss & Marcy relation), with only two adjacent pairs having values below 10. Out of 81 pairs, only 12 adjacent pairs have mutual Hill radii higher than that of the EPIC 212737443 system. All but one of the planet pairs contain either a ultra-short period planet ($P < 1$ day), a pair of super-Earth type planets or two planets with radii differing by more than $1 R_\oplus$. EPIC 212737443 is the only *K2* system with $\Delta R_H > 35$ including two planets with near-equal size. Weiss et al. (2018) concluded that there is a correlation between the radii of planets and the spacing between adjacent pairs. The implication of this correlation is that systems with similarly sized planets could potentially be direct remnants from the planet formation phase (Millholland et al. 2017). In terms of Hill radii, there is a lot of space in this system for a third planet to trace an orbit between planets *b* and *c*. Either a potential third planet is too small to be detected given the noise floor, could be a non-transiting planet (inclined orbit), or it could have been ejected from the system as a result of a past encounter event. We used MERCURY6 once again to place an $9 M_\oplus$ mass planet on a circular orbit between planets *b* and *c* to test the system stability. The simulation resulted in a stable configuration over 10^7 years, adding to the likelihood of a third planet. However, the sample of Kepler systems studied in Weiss et al. (2018) and our analysis of *K2* systems show that a majority of compact multi-planet systems contain planets of similar sizes. This means it is much more likely that another sub-Neptune sized planet lies between the validated planets, instead of a small planet that couldn't be detected. The implication here is that if a third planet exists, it is most likely to be non-transiting or have been ejected. Future follow-up observations will certainly be needed. However, the main issue for such observations is the faint nature of this star requiring a large aperture telescope.

7 SUMMARY

In conclusion, we used a light curve from the *K2* mission along with high resolution imaging to characterize and con-

¹⁰ <https://exoplanetarchive.ipac.caltech.edu/cgi-bin/TblView/nph-tblView>

¹¹ <http://www.openexoplanetcatalogue.com/systems/>

firm a system of two planets around EPIC 212737443. Planet *b* has an orbital period of (13.603 ± 0.0013) days and a radius of $(2.580 \pm 0.084) R_{\oplus}$, while planet *c* has a period of (65.550 ± 0.0089) days and a radius of $2.660 \pm 0.128 R_{\oplus}$. The radii of the two planets puts them firmly within the size regime of Sub-Neptune type planets. Their sizes imply that the planets are most likely gaseous, or contains significant amounts of volatiles such as water. The large mutual Hill radius of the system opens up the possibility for an additional planet of near-equal sizes between planets *b* and *c*. The study of systems with large values for ΔR_H such as EPIC 212737443, would add to the ongoing investigations of multi-planet systems to learn more about how planets are arranged and the implications for their formation histories.

ACKNOWLEDGMENTS

The authors would like to thank the anonymous referee for improving this research paper. MH, TCH, JHL and CTKL would like to thank the organizers of the Feb. 2018 Rencontres du Vietnam conference where this work was originally initiated. This paper includes data collected by the *Kepler/K2* mission. Funding for the *Kepler* mission is provided by the NASA Science Mission Directorate. This publication makes use of data products from the 1) WISE - Wide-field Infrared Survey Explorer, which is a joint project of the University of California, Los Angeles, and the Jet Propulsion Laboratory/California Institute of Technology, funded by the National Aeronautics and Space Administration; 2) SkyMapper - the national facility capability for SkyMapper has been funded through ARC LIEF grant LE130100104 from the Australian Research Council; 3) *Gaia* - This work has made use of data from the European Space Agency (ESA) mission *Gaia* (<https://www.cosmos.esa.int/gaia>), processed by the *Gaia* Data Processing and Analysis Consortium (DPAC, <https://www.cosmos.esa.int/web/gaia/dpac/consortium>). Funding for the DPAC has been provided by national institutions, in particular the institutions participating in the *Gaia* Multilateral Agreement; 4) Pan-STARRS - <https://panstarrs.stsci.edu/>. This publication makes use of 1) VOSA, developed under the Spanish Virtual Observatory project supported from the Spanish MICINN through grant AyA2011-24052; 2) the VizieR catalogue access tool, CDS, Strasbourg, France. The original description of the VizieR service was published in A&AS 143, 23; 3) DSS2 (<http://archive.eso.org/dss/dss>). Tobias C. Hinse would like to acknowledge a fruitful discussion with Dr. Eric Mamajek and Dr. Andrew Mann related to atmospheric properties of stars.

REFERENCES

Allard F., Homeier D., Freytag B., 2012, Philosophical Transactions of the Royal Society A: Mathematical, Physical and Engineering Sciences, 370, 2765
 Bailer-Jones C. A. L., 2015, PASP, 127, 994
 Baraffe I., et al., 2015, A&A, 577, 42
 Barros S. C. C., Demangeon O., Deleuil M., 2016, A&A, 594, 100
 Bayo A., et al., 2008, A&A, 492, 277
 Becker J.C., et al., 2018, preprint, (arXiv:1809.10688)
 Benneke B., et al., 2017, ApJ, 834, 187

Bensby T., Feltzing S., Lundström I., 2003, A&A, 410, 527
 Berardo D., et al. 2018, preprint, (arXiv:1809.11116)
 Borucki W. J., Koch D., Basri G., 2010, Science, 327, 977
 Caffau E., et al., 2011, Solar Physics, 268, 255
 Castelli F., Gratton R. G., Kurucz R. L., 1997, A&A, 318, 841
 Chambers J. E., 1999, MNRAS, 304, 793
 Chambers K. C., et al., 2016, <https://arxiv.org/abs/1612.05560>
 Claret A., Hauschildt P. H., Witte S., 2012, VizieR Online Data Catalog, 354
 Cosentino R., et al., 2012, in Ground-based and Airborne Instrumentation for Astronomy IV. p. 84461V, doi:10.1117/12.925738
 Crossfield I., et al., 2016, ApJS, 226, 7
 Cuntz M., Wang Z., 2018, RNAAS, 2a, 19
 Da Silva L., et al., 2006, A&A, 458, 609
 Dehnan W., Binney James J., 1998, MNRAS, 298, 387
 Dotter A., 2016, ApJS, 222, 11
 Dressing C. D., et al., 2017, ApJ, 836, 167
 Evans D. F., et al., 2016, A&A, 589, 58
 Evans D. F., et al., 2018, A&A, 610, 20
 Feroz F., et al., 2013, preprint, (arXiv:1306.2144)
 Fitzpatrick E. L., 1999, PASP, 111, 63
 Foreman-Mackey D., et al., 2013, PASP, 125, 306
 Gaia Collaboration et al., 2018b, A&A, 616, A10
 Giles H.A.C., et al., 2018, preprint, (arXiv:1806.08757)
 Girardi L., et al., 2005, A&A, 436, 895
 Gould A. & Morgan C. W., 2003, ApJ, 585, 1056
 Guo X., et al., 2017, ApJ, 838, 25
 Green G. M., et al., 2015, ApJ, 810, 25
 Huang C. X., et al., 2015, MNRAS, 454, 4159
 Hauschildt P. H., Allard F., Baron E., 1999, ApJ, 512, 377
 Herter T. L., et al. 2008, Proc. SPIE, Vol. 7014, Ground-based and Airborne Instrumentation for Astronomy II, 70140X
 Horch E. P., et al. 2009, AJ, 137, 5057
 Horch E. P., et al., 2012, AJ, 144, 165
 Horch E. P., et al. 2017, AJ, 153, 212
 Howell S. B., et al., 2011, AJ, 142, 19
 Howell S. B., et al., 2014, PASP, 126, 398
 Husser T. O., et al. 2013, A&A, 553, 6
 Huber D., et al., 2014, ApJS, 211, 2
 Huber D., et al., 2016, ApJS, 224, 2
 Kane S. R., Ciardi, D. R., Gelino, D. M., von Braun, K., 2012, MNRAS, 425, 757
 Kipping D. M., 2013, MNRAS, 435, 2152
 Koch D. G., et al. 2010, ApJL, 713, L131
 Kostov A., Bonev T., 2018, Bulgarian Astronomical Journal, 28, 3
 Kovacs G., Zucker S., Mazeh T., 2002, A&A, 391, 369
 Kreidberg L., 2015, PASP, 127, 1161
 Kupfer T., et al., 2018, MNRAS, 480, 302, private communication
 Lissauer J. J., et al., 2012, ApJ, 750, 112
 Luri X., et al., 2018, preprint, (arXiv:180409376L)
 Mandel K., Agol E., 2002, ApJ, 580, L171
 Mayo A. W., et al., 2018b, AJ, 155, 136
 Millholland S., Wang S., Laughlin G., 2017, ArXiv e-prints, arXiv:1710.11152
 Montet B. T., et al., 2015, ApJ, 809, 25
 Mortier A., et al., 2018, MNRAS, 481, 1839
 Morton T. D., 2015a, isochrones: Stellar model grid package, Astrophysics Source Code Library (ascl:1503.010)
 Morton T. D., 2015b, VESPA: False positive probabilities calculator, Astrophysics Source Code Library (ascl:1503.011)
 Ofir A. 2014, A&A, 561, A138
 Pepe F., et al., 2010, Proc. SPIE 7735, 77350F, PSISDG0277-786X, <http://dx.doi.org/10.1117/12.857122>
 Pope B. J. S., Parviainen H., Aigrain S., 2016, MNRAS, 461, 3399
 Reddy B. E., Lambert D. L., Allende Prieto C., 2006, MNRAS, 367, 1329

- Scott N. J., Howell S. B., Horch E. P., 2016, in Proc. SPIE, Vol. 9907, Optical and Infrared
- Sharma S., et al., 2011, ApJ, 730, 3
- Siess L., Dufour E., Forestini M., 2000, A&A, 358, 593
- Skottfelt J., et al., 2015, A&A, 574, 54
- Skrutskie M. F., et al., 2006, AJ, 131, 1163
- Soubiran C., Bienaymé O., Siebert A. 2003, A&A, 398, 141
- Tonry J. L., et al., 2012, ApJ, 750, 99
- Van Eylen V. & Albrecht S., 2015, ApJ, 808, 126
- Vanderburg A. & Johnson J. A., 2014, PASP, 126, 948
- Vanderburg A., et al., 2016, ApJ, 827, L10
- Weiss L. M., Marcy G. W., 2014, ApJ, 783, L6
- Weiss L. M., et al., 2018, AJ, 155, 48
- Wisdom. J., 1980, AJ, 85, 1122
- Wolfgang A., Rogers L. A., Ford E. B., 2016, ApJ, 825, 19
- Wolf C., et al., 2018, PASA, 35, 10
- Wright E. L., et al., 2010, AJ, 140, 1868